Hydrogen-Bond Reinforced Superstructural Manganese Oxide As the Cathode for Ultra-Stable Aqueous Zinc Ion Batteries

Jianwei Li, Ningjing Luo, Liqun Kang, Fangjia Zhao, Yiding Jiao, Thomas J. Macdonald, Min Wang, Ivan P. Parkin, Paul R. Shearing, Dan J.L. Brett, Guoliang Chai,* and Guanjie He*

Layered manganese oxides adopting pre-accommodated cations have drawn tremendous interest for the application as cathodes in aqueous zinc-ion batteries (AZIBs) owing to their open 2D channels for fast ion-diffusion and mild phase transition upon topochemical (de)intercalation processes. However, it is inevitable to see these "pillar" cations leaching from the hosts owing to the loose interaction with negatively charged Helmholtz planes within the hosts and shearing/bulking effects in 2D structures upon guest species (de)intercalation, which implies a limited modulation to prevent them from rapid performance decay. Herein, a new class of layered manganese oxides, $Mg_{0.9}Mn_3O_7 \cdot 2.7H_2O$, is proposed for the first time, aims to achieve a robust cathode for high-performance AZIBs. The cathode can deliver a high capacity of 312 mAh g^{-1} at 0.2 A g^{-1} and exceptional cycling stability with 92% capacity retention after 5 000 cycles at 5 A g^{-1}. The comprehensive characterizations elucidate its peculiar motif of pined Mg-□Mn-Mg dumbbell configuration along with interstratified hydrogen bond responsible for less Mn migration/dissolution and quasi-zero-strain characters. The revealed new structure-function insights can open up an avenue toward the rational design of superstructural cathodes for reversible AZIBs.

1. Introduction

In consideration of increasingly severe carbon emission issues and rigid stipulations for low-carbon society objectives, cur-

rent electrochemical energy storage systems require a radical upgrade to meet various application demands from end users. Aqueous zinc-ion batteries (AZIBs) provide sustainable routes to grid-scale energy storage systems because of their cost and safety advantages by using mild aqueous electrolytes and abundant metallic zinc anodes.[1] Besides, owing to distinctive merits such as relatively high ionic conductivity, environmental benignity, low risks of flammability, and considerable energy density of AZIBs compared with conventional Li-ion batteries, AZIBs are intensively investigated to unleash the potential for practical applications.[2] However, as essential components governing the entire performance of batteries, cathode materials are still suffering from limited promising candidates possessing staid topological features.[3] Among them, vanadium-based, manganese-based, and Prussian blue analogs-based materials were widely studied.[4] By comparison of these cathodes, it should be emphasized that even though vanadium-based materials exhibit superb rate capability and relatively large capacity, the low working voltage plateau (≈0.7 V vs Zn^{2+}/Zn) and relatively high cost of raw materials substantially

J. Li, N. Luo, G. Chai
State Key Laboratory of Structural Chemistry
Fujian Institute of Research on the Structure of Matter
Chinese Academy of Sciences (CAS)
Fuzhou, Fujian 350002, P.R. China
E-mail: g.chai@fjirsm.ac.cn
J. Li, T. J. Macdonald, G. He
School of Engineering and Materials Science
Queen Mary University of London
London E1 4NS, UK

The ORCID identification number(s) for the author(s) of this article can be found under https://doi.org/10.1002/aenm.202201840.

L. Kang, P. R. Shearing, D. J.L. Brett, G. He
Department of Chemical Engineering
University College London
London WC1E 7JE, UK
E-mail: g.he@ucl.ac.uk
F. Zhao, Y. Jiao, I. P. Parkin
Department of Chemistry
University College London
20 Gordon Street, London WC1H 0AJ, UK
M. Wang
Key Laboratory of Comprehensive and Highly Efficient Utilization of Salt Lake Resources
Qinghai Institute of Salt Lakes
Chinese Academy of Sciences (CAS)
Xining 810008, P.R. China

**ADVANCED
SCIENCE NEWS**
www.advancedsciencenews.com

**ADVANCED
ENERGY
MATERIALS**
www.advenergymat.de

hinder their development prospect.[5] While Prussian blue analogues can deliver the highest working voltage plateau (normally > 1.4 V vs Zn^{2+}/Zn) and feasibility of mass production, the poor cycling stability and low theoretical capacity (<200 mAh g^{-1} at low current densities) are obvious drawbacks compared with others.[6] Therefore, manganese-based cathodes come under the spotlight due to satisfactory voltage plateaus and specific capacity.[7] In particular, δ-MnO_2 materials with layered structures are the most promising hosts compared to other tunneled MnO_2 polymorphs, such as α-MnO_2 (2 × 2 tunnels), β-MnO_2 (1 × 1 tunnels), γ-MnO_2 (1 × 2 and 1 × 1 tunnels), λ-MnO_2 (1 × 3 tunnels) due to a large d-space (≈0.7 nm) between MnO_6 octahedra formed two-dimensional (2D) slabs and relatively less phase transition during charge storage processes.[8] Nevertheless, this type of cathode is still challenged by inferior cycling stability, sluggish reaction kinetics, and fast capacity attenuation because of dramatic volume changes, structural disorder, and Mn^{2+} dissolution.[9–11]

Many attempts of modifying pristine δ-MnO_2 have been proposed including defect engineering, pre-intercalated guest species, and compositing with electrically conductive agents, delivering enhancements on battery performance to some extent.[12] For instance, the pre-intercalation strategy is one of the most acknowledged methods to tune intrinsic properties of δ-MnO_2 hosts via reconstruction of electronic structures and reinforcement of interlayer interactions.[13,14] Meanwhile, bounded water of guest species can provide shielding effects by reducing electrostatic positive charges with apical oxygen within the host frameworks. As a consequence, electrical conductivity, diffusion kinetics, and structural stability can be effectively improved.[15,16] Nevertheless, there are two scientific facts which are easily neglected in previous studies on the pre-intercalation strategy of δ-MnO_2. First, intrinsic ion-exchangeable properties of δ-MnO_2 hosts have been revealed iteratively.[17–20] In other words, the "pillar" ions can be replaced by various cations due to the feeble electrostatic interactions on Helmholtz planes.[21] It is conceivable that the merits of enhanced electrochemical performances derived from deliberately introduced "pillars" could hardly be stable especially when confronted with rich Zn^{2+} and protons. Second, the irreversible phase transformation induced by shearing and buckling effects of transition metal oxide layers is the culprit responsible for the structural failure during (dis)charge processes for AZIBs, but which was not discussed thoroughly.[22,23] Hence, the innovation of crystallographic structures is urgently needed to bring substantial progress for reversible AZIBs cathodes.

To overcome these issues, state-of-the-art cathode materials regarding new configurations of Mn–O motif and enhanced interlayer interactions are promising for less phase changes and inhibited distortion/dissolution during (de)intercalation processes.[24] As a proof of concept, a new superstructural 2D manganese oxide, $Mg_{0.9}Mn_3O_7\cdot2.7H_2O$, is first-time proposed to gain extraordinary battery performance. More specific, the high specific capacities of 312 mAh g^{-1} and 132 mAh g^{-1} at 0.2 A g^{-1} and 5 A g^{-1}, respectively, along with a 92% capacity retention after 5000 cycles can be achieved. Meanwhile, through in/ex situ experimental and theoretical comparison of structural/chemical evolutions and electrochemical properties among conventional layered manganese oxides (δ-$Mg_2Mn_{14}O_{27}\cdot nH_2O$, δ-$MnO_2\cdot nH_2O$ and δ-$Na_{0.55}Mn_2O_4\cdot2.4H_2O$) and

$Mg_{0.9}Mn_3O_7\cdot2.7H_2O$, the advantages of superstructural cathode materials are discussed in detail. It is revealed that a microstructure-governed performance improvement originated from specific 2D features of reticular MnO_6 and MgO_6 chains along with built-in Mn vacancy, which endows hydrogen bond stabilized layered structure and horizontal pinning effects on transition metal layers. As the result, the robust framework with less Mn migration and quasi-zero lattice volume changes contributes to superior electrochemical performance compared with previously reported manganese-based cathodes. Overall, these findings provide new insights of developing superstructures of layered transition metal oxides for reversible AZIBs.

2. Result and Discussion

2.1. Structural Evaluation of Pristine Layered Manganese Oxides

$Mg_{0.9}Mn_3O_7\cdot2.7H_2O$ was prepared by a single-step hydrothermal reaction (see experimental section). While δ-$Na_{0.55}Mn_2O_4\cdot2.4H_2O$ was fabricated by the room-temperature coprecipitation method. Other δ-phase manganese oxides with pre-intercalated Mg^{2+} and proton were carried out via a simple ion-exchange process by immersing pristine δ-$Na_{0.55}Mn_2O_4\cdot2.4H_2O$ in 1 M $MgNO_3$ and HNO_3 solutions, respectively, to obtain δ-$Mg_2Mn_{14}O_{27}\cdot nH_2O$ and δ-$MnO_2\cdot nH_2O$, respectively. The morphology of $Mg_{0.9}Mn_3O_7\cdot2.7H_2O$ was characterized by a typical scanning electron microscope (SEM), which depicted petal-like flakes with nanoscale thickness as shown in **Figure 1**a. In comparison, δ-$Na_{0.55}Mn_2O_4\cdot2.4H_2O$ and their derivatives exhibit different morphologies of wrinkled layers (Figure 1b and S1, Supporting Information). Meanwhile, energy dispersive X-ray spectroscopy (EDS) mapping images of the derivatives confirmed that no Na residue was left after ion-exchange treatment, implying the fact of inherent properties of δ-MnO_2 hosts as mentioned above. Additionally, the features of surface areas were not only determined by gas adsorption approach on pristine powders, but evaluated by electrochemically active surface area (ECSA) on as-prepared electrodes of δ-$Mg_2Mn_{14}O_{27}\cdot nH_2O$ and $Mg_{0.9}Mn_3O_7\cdot2.7H_2O$, respectively, to correlate intrinsic properties of materials with their corresponding electrochemical reactions. It is seen that Brunauer–Emmett–Teller specific surface areas of δ-$Mg_2Mn_{14}O_{27}\cdot nH_2O$ and $Mg_{0.9}Mn_3O_7\cdot2.7H_2O$ are 129.06 m^2 g^{-1} and 74.29 m^2 g^{-1} along with dominated pore sizes of ≈24.2 nm and ≈51.4 nm, respectively (Figure S2, Supporting Information). Although the geometric surface area of the pristine powders showed distinguishable differences, the results of ECSA verify that the electrodes actually possess comparable double-layer capacitance of 15.12 mF cm^{-2} and 11.84 mF cm^{-2} for δ-$Mg_2Mn_{14}O_{27}\cdot nH_2O$ and $Mg_{0.9}Mn_3O_7\cdot2.7H_2O$, respectively, which are both higher than that of commercial MnO_2 electrodes (9.37 mF cm^{-2}) measured under identical conditions (Figure S3, Supporting Information).The powder X-ray diffraction (PXRD) patterns of $Mg_{0.9}Mn_3O_7\cdot2.7H_2O$ can be corresponded to ICSD No.239225 referring to Jianshuiite mineral database with a chemical formula of $MgMn_3O_7\cdot3H_2O$ as shown in Figure 1c.[25] The Rietveld-refinement crystal diffraction profiles further verified that the as-prepared $Mg_{0.9}Mn_3O_7\cdot2.7H_2O$ possess the same space group of $R\overline{3}$ with slightly reduced lattice
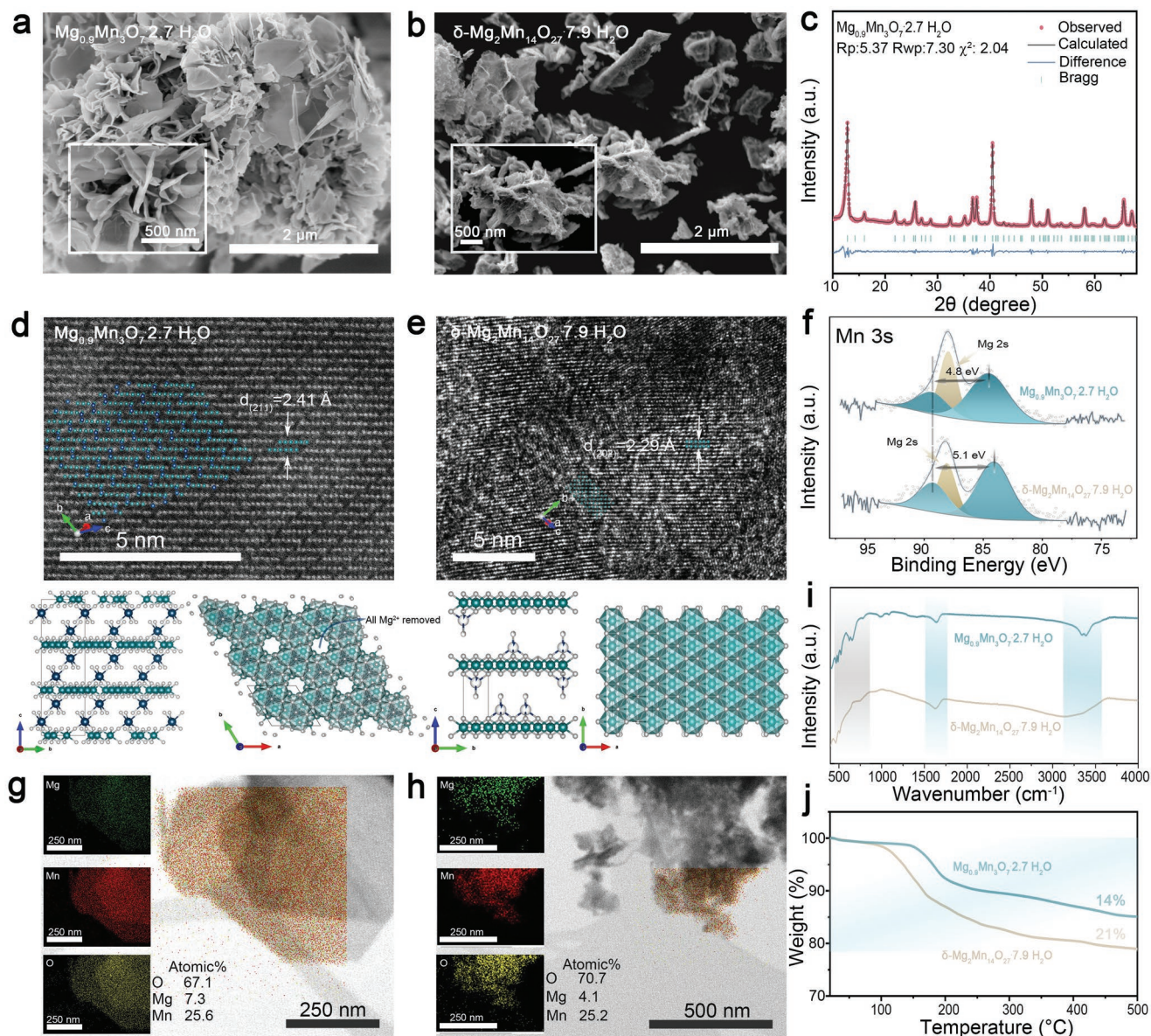
Figure 1. Structural and morphological characterizations of $Mg_{0.9}Mn_3O_7 \cdot 2.7H_2O$ and $\delta\text{-}Mg_2Mn_{14}O_{27} \cdot 7.9H_2O$: a, b) SEM images. c) Rietveld-refined crystal diffraction profiles. d,e) HAADF-STEM images along with stacking models of corresponding crystallographic structures. (Dark green, dark blue and small grey spheres refer to Mn, Mg, and O atoms; all Mg^{2+} were removed from stacking mode along (c-axis) top view in $Mg_{0.9}Mn_3O_7 \cdot 2.7H_2O$). f) XPS profiles of Mn 3s. i) FTIR spectra. j) TGA curves.

parameters ($a = b = 7.534(4)$ Å, $c = 20.767(2)$ Å, $\alpha = \beta = 90°$, $\gamma = 120°$) compared with the standard material, especially for the c lattice constant which reflects a decreased d-spacing along [001] direction from 6.93 Å to 6.86 Å. This phenomenon can be interpreted by forming Mg vacancy in the pristine material and will be discussed in detail in the following content. Additionally, the scheme of the conjectural crystallographic structure of $Mg_{0.9}Mn_3O_7 \cdot 2.7H_2O$ supercell projected from different orientations was demonstrated in Figure S4a, Supporting Information. The XRD patterns of $\delta\text{-}Mg_2Mn_{14}O_{27} \cdot nH_2O$, $\delta\text{-}MnO_2 \cdot nH_2O$, and $\delta\text{-}Na_{0.55}Mn_2O_4 \cdot nH_2O$ can be viewed in Figure S4b, Supporting Information, in which all diffraction peaks are in good conformity with a standard database of JCPDS No.50-0014 Buserite, ICSD No. 187 580 H-Birnessite and ICSD No. 68 916

Na-Birnessite, respectively, suggesting pure phases were successfully attained by ion-exchange methods. Among them, $\delta\text{-}Mg_2Mn_{14}O_{27} \cdot nH_2O$ exhibits the largest interlayer spacing of 9.64 Å compared with 7.38 Å and 7.12 Å of $\delta\text{-}MnO_2 \cdot nH_2O$ and $\delta\text{-}Na_{0.55}Mn_2O_4 \cdot nH_2O$, respectively, due to more water coordination within the interlayer of the framework. Additionally, further identification of different microstructures was carried out by an aberration-corrected scanning transmission electron microscopy (AC-STEM) in which the contrast in high-angle annular dark-field images is varied on the basis of atomic numbers according to a $Z^{1.7}$ dependency (Z-contrast imaging),[26] and hence, more sensitive to heavy atoms such as Mn in this study. The HAADF-STEM/High-resolution TEM images of $Mg_{0.9}Mn_3O_7 \cdot 2.7H_2O$ and $\delta\text{-}Mg_2Mn_{14}O_{27} \cdot nH_2O$

**ADVANCED
SCIENCE NEWS**
www.advancedsciencenews.com

**ADVANCED
ENERGY
MATERIALS**
www.advenergymat.de

were presented in Figure 1d,e, respectively, to demonstrate divergent geometric orders of Mn–O layers. Intriguingly, it is clearly observed that the $Mg_{0.9}Mn_3O_7 \cdot 2.7H_2O$ possesses a special Mn atom arrangement reflecting as periodical six-atom in a line divided by a vacancy involving Mg–□Mn–Mg dumbbells structure. In contrast, δ-$Mg_2Mn_{14}O_{27} \cdot nH_2O$ shows conventional ribbon orders of Mn with no intervals. Most importantly, through a comparison of stacking models (side and top views) of these two manganese oxides, both layered structures can be identified. However, the geometric orders of stacked layers are highly different to each other. Specifically, the unit cell of $Mg_{0.9}Mn_3O_7 \cdot 2.7H_2O$ can be subdivided into Mg^{2+} layers and $Mn_3O_7 = Mn_{6/7}O_2$ ($[□_{1/7}Mn^{4+}_{6/7}]$) layers which stack together alternatively.[27] Meanwhile, it is seen from the top view that an ordered □-Mn arrangement formed in the layer due to the regularly depleted Mn surrounded by triangular MnO_6 octahedra combinations giving rise to constructing an intrinsic Mn vacancy. Furthermore, Mg^{2+} is pinned above and below the vacancy and coordinated with hydrated water molecules. As for δ-$Mg_2Mn_{14}O_{27} \cdot nH_2O$, a small amount of pre-intercalated ions and hydrated water molecules form a complex interlayer coordination within MnO_2 slabs. As a result, we speculate that these different superstructural manganese oxides could have significant modulation on their electrochemical properties because of different "pillar" ion stability and allotropic forms of MnO_6 octahedra.

Additionally, the surface chemical information of as-prepared $Mg_{0.9}Mn_3O_7 \cdot 2.7H_2O$ and δ-$Mg_2Mn_{14}O_{27} \cdot nH_2O$ were carried out by X-ray photoelectron spectroscopy (XPS) as shown in Figure 1f and S4c,d, Supporting Information. The deconvolution of core level spectra of Mn 3s clearly identifies the only Mn^{4+} species existing in $Mg_{0.9}Mn_3O_7 \cdot 2.7H_2O$, while there is partial reduction of valence states of Mn^{4+} in δ-$Mg_2Mn_{14}O_{27} \cdot 7.9H_2O$, reflected by a relatively higher magnitude of peak splitting of 5.1 eV compared with 4.8 eV in $Mg_{0.9}Mn_3O_7 \cdot 2.7H_2O$. The phenomena of oxidation states also are in good accordance with previously reported pre-intercalated δ-MnO_2.[28,29] Moreover, the core level spectra of Mg and survey spectra further confirm that only Mg^{2+} species exist in both Mg pre-intercalated MnO_2 materials. Through XPS and TEM-EDS analysis (Figure 1g,h), it is indicated that the chemical formulas of these two pristine materials are $Mg_{0.9}Mn_3O_7 \cdot 2.7H_2O$ and δ-$Mg_2Mn_{14}O_{27} \cdot 7.9H_2O$, which also proves a small amount of Mg vacancy generated in $Mg_{0.9}Mn_3O_7 \cdot 2.7H_2O$ during the synthesis. The profiles derived from Fourier transform infrared (FTIR) spectroscopy in Figure 1f confirm that both layered materials possess water molecules manifested as distinguished O–H bending and H—O–H stretching vibration modes at ≈ 1600 cm^{-1} and 3200–3500 cm^{-1}, respectively.[30] The thermogravimetric analysis (TGA) was equipped to determine the weight percentage of lattice/absorbed water as shown in Figure 1j. The weight loss of 14% and 21% for $Mg_{0.9}Mn_3O_7 \cdot 2.7H_2O$ and δ-$Mg_2Mn_{14}O_{27} \cdot 7.9H_2O$, respectively, can be observed in a temperature range from $100 \approx 500$ °C, and relatively higher dehydration temperature suggest higher thermodynamic stability of the lattice water in $Mg_{0.9}Mn_3O_7 \cdot 2.7H_2O$, which could deliver steady charge shielding effect for fast charge diffusion.

2.2. Battery Performance Evaluation

To assess the AZIB performance of $Mg_{0.9}Mn_3O_7 \cdot 2.7H_2O$ and pre-intercalated δ-MnO_2 cathodes, coin-type and Swagelok cells are assembled for the electrochemical performance evaluations. **Figure 2**a presents galvanostatic charge-discharge (GCD) profiles of $Mg_{0.9}Mn_3O_7 \cdot 2.7H_2O$ and δ-$Mg_2Mn_{14}O_{27} \cdot 7.9H_2O$ under stepwise increased charge/discharge current densities from 0.2 to 5 A g^{-1}. The less plateaus changes upon elevated current densities can be observed in $Mg_{0.9}Mn_3O_7 \cdot 2.7H_2O$ cathodes along with a relatively higher specific capacity under each current density compared with those in δ-$Mg_2Mn_{14}O_{27} \cdot 7.9H_2O$. Similarly, more steady cyclic voltammetry (CV) curves after initial cyclic activation in Figure 2b clearly indicate that better redox reaction kinetic behaviors were gained in $Mg_{0.9}Mn_3O_7 \cdot 2.7H_2O$ due to less polarization reflecting as relatively small potential differences (308, 230 mV versus 375, 262 mV in δ-$Mg_2Mn_{14}O_{27} \cdot 7.9H_2O$) between two pairs of cathodic and anodic peaks. Therefore, the rate performance of these two cathodes exhibits distinct features especially under high current densities, i.e., a series of average specific capacities of 312, 282, 245, 195, 164, and 132 mAh g^{-1} were achieved in $Mg_{0.9}Mn_3O_7 \cdot 2.7H_2O$ compared with 285, 231, 199, 157, 130, and 101 mAh g^{-1} in δ-$Mg_2Mn_{14}O_{27} \cdot 7.9H_2O$ at current densities of 0.2, 0.5, 1, 2, 3, and 5 A g^{-1}, respectively. **Figure 3**d,e displays the comparison of long cycling stability evaluations on $Mg_{0.9}Mn_3O_7 \cdot 2.7H_2O$ and δ-$Mg_2Mn_{14}O_{27} \cdot 7.9H_2O$ at 0.2 A g^{-1} and 5 A g^{-1}, respectively, in which relatively higher capacity retention performances (against 2nd cycled capacities) of 95% and 92% of $Mg_{0.9}Mn_3O_7 \cdot 2.7H_2O$ were achieved along with specific capacities of 272 and 94 mAh g^{-1} after 100 and 5000 cycles, respectively, in contrast to only 82% and 80% of δ-$Mg_2Mn_{14}O_{27} \cdot 7.9H_2O$ under the identical conditions along with final specific discharge capacities of 199 mAh g^{-1} and 65 mAh g^{-1}, respectively. Similarly, CV and GCD measurements of δ-$Na_{0.55}Mn_2O_4 \cdot 2.4H_2O$ and δ-$MnO_2 \cdot nH_2O$ were also conducted to demonstrate "pillar" effects on the battery performance as shown in Figure S5, Supporting Information. It is seen that all δ-phase MnO_2 cathodes present similar CV curve characters but slightly different response currents of relative magnitude between two pairs of redox-active peaks, implying different charge storage properties related to H$^+$ and Zn^{2+} co-(de)intercalation reported before.[31] Wang and co-works suggested that the high voltage plateau are dominantly controlled by H$^+$ insertion/extrusion due to relatively small hydrated radius, whereas the low voltage plateau are governed by Zn^{2+} insertion/extrusion manifesting a relative sluggish diffusion kinetics.[32] Therefore, δ-$Mg_2Mn_{14}O_{27} \cdot 7.9H_2O$ exhibits the largest magnitude of current responses at low voltage plateau rather than the other two δ-phase MnO_2, which could be inferred by an enhanced Zn^{2+} diffusion kinetics due to the largest interlayer spacing. These results are in good accordance with previous studies on interlayer spacing modulation to improve reaction kinetics.[33,34] Additionally, with pillar effects enhancement, the long cycling performance of δ-$Na_{0.55}Mn_2O_4 \cdot nH_2O$ is superior to that of δ-$MnO_2 \cdot nH_2O$ reflecting as good capacity retention of 68% against 39%, respectively, after 100 (dis)charge processes at the current density of 0.2 A g^{-1}, and 72% against 32%, respectively, after 5000 cycling tests at 5 A g^{-1}. Intriguingly, it is seen
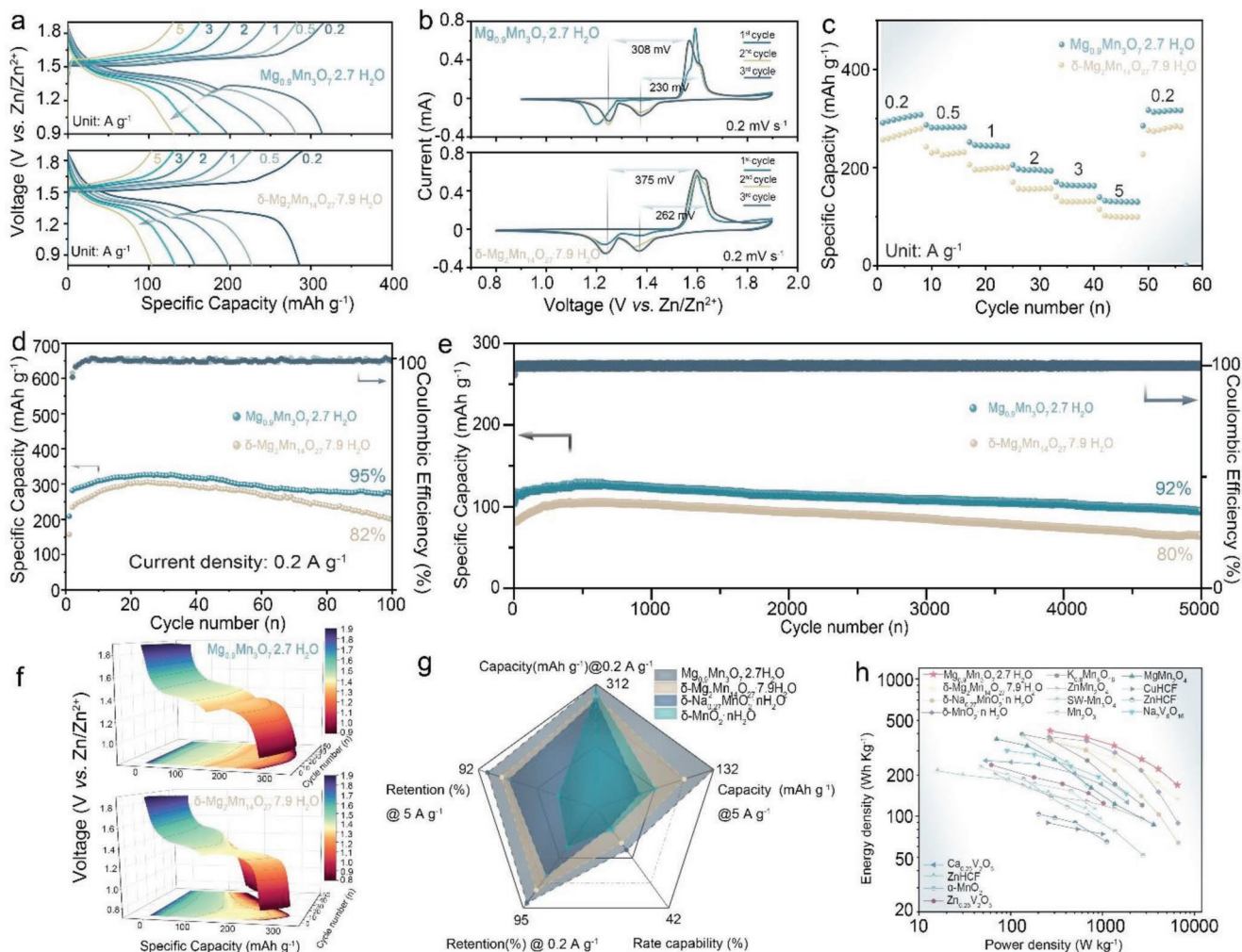
Figure 2. Comparison of battery performance for $Mg_{0.9}Mn_3O_7 \cdot 2.7H_2O$ and $\delta\text{-}Mg_2Mn_{14}O_{27} \cdot 7.9H_2O$: a) GCD curves. b) CV profiles. c) Rate performance. d,e) Cycling performance at current densities of 200 and 5000 mA g^{-1}, respectively. f) Galvanostatic discharge curves. g) Radar diagram of overall comparison of battery performance between $Mg_{0.9}Mn_3O_7 \cdot 2.7H_2O$ and $\delta\text{-}MnO_2$. h) Ragone plot of as-obtained MnO_2 (the total mass of active materials) compared with reported cathode materials.

that there is remarkable capacity decay of all δ-phase MnO_2 even though some of them delivered "pillar effect" protection from structural collapse. Meanwhile, these unsatisfied cycling stabilities of δ-phase MnO_2 cathodes are also verified by many previous studies (Table S1, Supporting Information), giving rise to concerns about their structural stability.

To disclose the nature of rapid capacity decay of $\delta\text{-}Mg_2Mn_{14}O_{27} \cdot 7.9H_2O$ cathode, GCD curves by 50 cycles of charge/discharge treatment under a low current density (100 mA g^{-1}) were carried out for both Mg^{2+} pre-intercalated MnO_2. Obviously, both cathodes have two distinct discharge plateaus (DPs) which are divided by a tuning point ≈1.35 V referring to different stages of charge storage. Upon the initial activation process of both cathodes, two DPs increase dramatically as shown in the blue-green and yellow-red regions in Figure 2f. With proceeding the cycling measurements, the specific capacity of low DP (<1.35 V) in $\delta\text{-}Mg_2Mn_{14}O_{27} \cdot 7.9H_2O$ displays a significant drop from the initial 106 mAh g^{-1} to 47 mAh g^{-1} compared with that (134 mAh g^{-1} to 92 mAh g^{-1})

of $Mg_{0.9}Mn_3O_7 \cdot 2.7H_2O$, while the specific capacity of high DPs in both cathodes are relatively reversible. This phenomenon can be speculated as an irreversible feature of the δ-phase host for Zn^{2+} intercalation, which will be proved in structural evolution in the following section. To better compare the battery performance among $Mg_{0.9}Mn_3O_7 \cdot 2.7H_2O$ and other as-prepared δ-phase MnO_2, a radar diagram consisting of five parameters in terms of maximum specific capacities, rate capabilities, capacity retentions after 100 and 5000 cycles, respectively. The comprehensive comparisons indicate that $Mg_{0.9}Mn_3O_7 \cdot 2.7H_2O$ has the overwhelming electrochemical performance among all investigated samples. Considering the positive influence of $MnSO_4$ additives on cycling stability and interfacial properties of cathodes, additional GCD measurements adopting only 3 M $ZnSO_4$ aqueous electrolyte were carried out to inspect their cycling performances. It is seen that the $Mg_{0.9}Mn_3O_7 \cdot 2.7H_2O$ cathode can still maintain 73% capacity after 100 cycles at a low current density of 200 mA g^{-1}, which is obviously superior to 55% of $\delta\text{-}Mg_2Mn_{14}O_{27} \cdot 7.9H_2O$ cathode at identical conditions

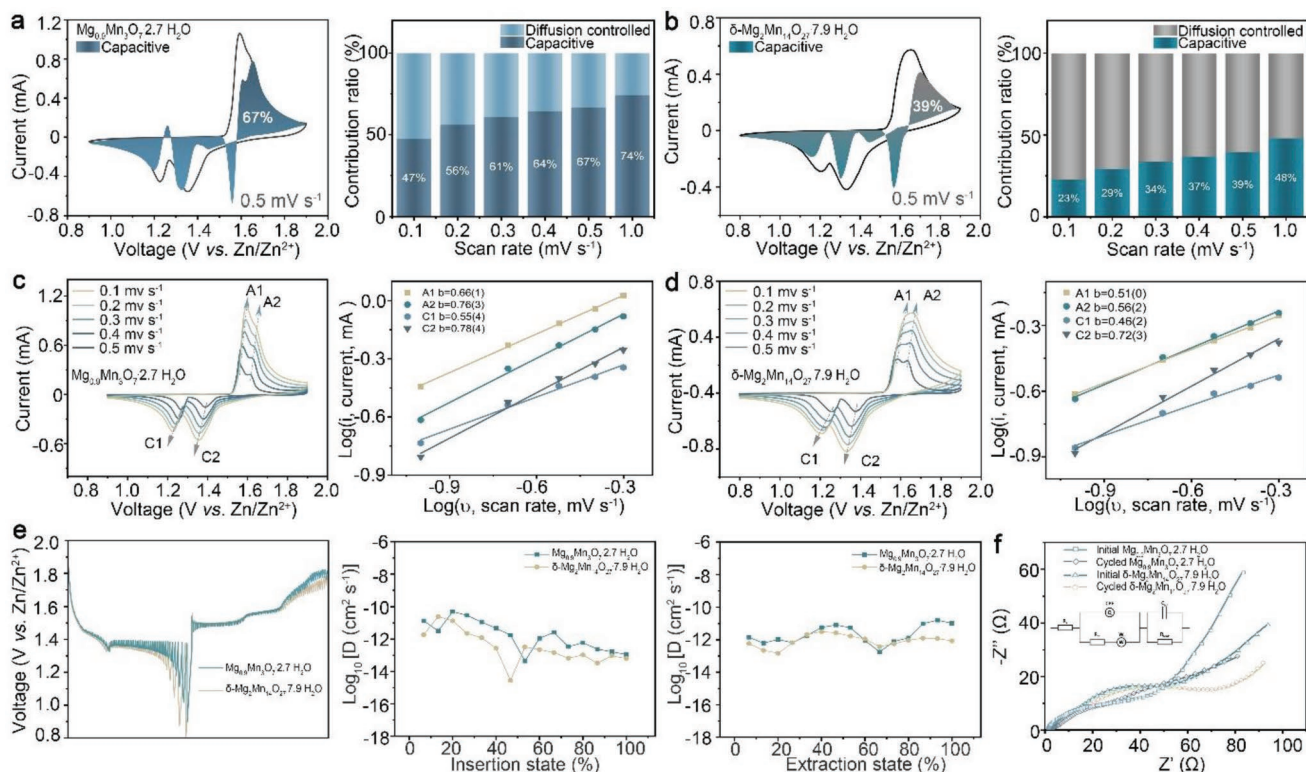**Figure 3.** a,b) Capacitive contributions and c,d) CV profiles of $Mg_{0.9}Mn_3O_7 \cdot 2.7H_2O$ and $\delta\text{-}Mg_2Mn_{14}O_{27} \cdot 7.9H_2O$ at varied sweep rates, respectively. e) GITT profiles with the comparison of diffusion coefficients and f) EIS characterizations of $Mg_{0.9}Mn_3O_7 \cdot 2.7H_2O$ and $\delta\text{-}Mg_2Mn_{14}O_{27} \cdot 7.9H_2O$, respectively.

(Figure S6a, Supporting Information). Meanwhile, the corresponding GCD curves of these cycling measurements also confirm varied attenuation behaviors of two DPs between these materials which further indicates a better reversibility of $Mg_{0.9}Mn_3O_7 \cdot 2.7H_2O$ (Figure S6b,c, Supporting Information). Furthermore, the energy/power density (based on the total mass of active materials on the cathode) of $Mg_{0.9}Mn_3O_7 \cdot 2.7H_2O$, $\delta\text{-}Mg_2Mn_{14}O_{27} \cdot 7.9H_2O$, $\delta\text{-}Na_{0.55}Mn_2O_4 \cdot nH_2O$, $\delta\text{-}MnO_2 \cdot nH_2O$ along with previously reported state-of-the-art MnO_2,[35–40] V_2O_5[41–43] and PBAs[44–46] based cathodes are summarized in the Ragone plot as shown in Figure 2h, which illustrate outstanding energy/power densities of $Mg_{0.9}Mn_3O_7 \cdot 2.7H_2O$ were gained as high as 418.4 Wh kg^{-1}/6.5 kW kg^{-1} for AZIBs.

2.3. Kinetic Behaviors

To reveal underlying mechanisms of promoted electrochemical performances of $Mg_{0.9}Mn_3O_7 \cdot 2.7H_2O$ compared with $\delta\text{-}Mg_2Mn_{14}O_{27} \cdot 7.9H_2O$, the electrochemical reaction kinetics were characterized by CV analysis, galvanostatic intermittent titration technique (GITT) and electrochemical impedance spectroscopy (EIS). Figure 3a shows the CV profile of $Mg_{0.9}Mn_3O_7 \cdot 2.7H_2O$ with a 67% capacitive contribution at a sweep rate of 0.5 mV s^{-1}. Moreover, with the stepwise growth of sweep rates from 0.1 to 1 mV s^{-1}, it is seen that the fraction of capacitive contribution of $Mg_{0.9}Mn_3O_7 \cdot 2.7H_2O$ can increase from 47% to 74%. Comparatively, $\delta\text{-}Mg_2Mn_{14}O_{27} \cdot 7.9H_2O$ only presents capacitive contribution ratios increased from 23% to

48% under identical conditions (Figure 3b). These results indicate that the kinetics of $\delta\text{-}Mg_2Mn_{14}O_{27} \cdot 7.9H_2O$ are mainly determined by diffusion-controlled processes especially under low sweep rates, whereas the capacitive charge storage behaviors become increasingly dominated as the growth of sweep rates for $Mg_{0.9}Mn_3O_7 \cdot 2.7H_2O$, suggesting a fast kinetics for this cathode material. Additionally, CV curves of $Mg_{0.9}Mn_3O_7 \cdot 2.7H_2O$ and $\delta\text{-}Mg_2Mn_{14}O_{27} \cdot 7.9H_2O$ were collected at varied scan rates from 0.1 to 1 mV s^{-1} (Figure 3c,d). Notably, two pairs of redox peaks (C1 and C2) at various cathodic sweeps of both materials are distinguishable, but the evolution tendency of C1/C2 and A1/A2 ratios is different upon increasing sweep rates due to the limited Zn^{2+} transfer kinetics of $\delta\text{-}Mg_2Mn_{14}O_{27} \cdot 7.9H_2O$, which is consistent with GCD profiles. Meanwhile, homologous processes of charge storage can be discerned by the linear relationship for log i versus log v using the equation[47]:

$$i = av^b \tag{1}$$

Where the peak current i and sweep rate v can be readable and a, b are adjustable parameters. The value of b within a range of $0.5 - 1$ indicates different charge storage behaviors with respect to capacitive ($b = 1$) and diffusion-controlled ($b = 0.5$) mechanisms. Therefore, linear fitted b values of both cathodes are conformably fallen into a scope between 0.5 and 0.8 according to well-defined anodic/cathodic peaks from the plots, which implies their electrochemical reaction behaviors are governed by both diffusion-controlled and capacitive processes. The higher b values (0.66, 0.76, 0.55, and 0.78)

of $Mg_{0.9}Mn_3O_7 \cdot 2.7H_2O$ can be clearly identified, revealing an enhanced contribution of response current from capacitance compared with the solid-state diffusion-dominated feature of δ-$Mg_2Mn_{14}O_{27} \cdot 7.9H_2O$. These capacitive behaviors can be ascribed to the relatively more pseudocapacitive charge storage capability suggesting inherently rapid reaction kinetics as for $Mg_{0.9}Mn_3O_7 \cdot 2.7H_2O$.

Additionally, the solid-state diffusion kinetics of both Mg-involved manganese oxides were evaluated by GITT as shown in Figure 3e, in which the straightaway voltage drop/rise after applied galvanostatic current can be regarded as the uncompensated charge transfer resistance, following with the gradual voltage change during the relaxation period which associates with the ion diffusion process. Hence, there is a remarkable difference in the overpotential values between two DPs which are attributed to the dissimilarity of ion diffusion properties related to proton and Zn^{2+} dominated insertion/extrusion reactions, agreeing well with the reported H^+ and Zn^{2+} co-insertion system. Moreover, a relatively higher diffusion coefficient ($\approx 10^{-10}$ to 10^{-13} m^2s^{-1}) of $Mg_{0.9}Mn_3O_7 \cdot 2.7H_2O$ compared with that ($\approx 10^{-11}$ to 10^{-14} m^2s^{-1}) of δ-$Mg_2Mn_{14}O_{27} \cdot 7.9H_2O$ further prove the improved kinetics in the superstructural manganese oxide. In addition to GITT analysis, EIS characterizations were carried out to determine their charge-transfer features and ion-diffusion kinetics upon initial and fully charged states after cycling tests of two electrodes. Figure 3f presents a typical equivalent circuit with fitted Nyquist plots to demonstrate their Ohmic resistance (R_s) and Faradaic interfacial charge transfer resistance (R_{ct}). It is seen that $Mg_{0.9}Mn_3O_7 \cdot 2.7H_2O$ electrode possesses smaller R_s (initial state: 0.5 Ω and cycled state: 0.88 Ω) than those (initial state: 0.75 Ω and cycled state: 1.04 Ω) of δ-$Mg_2Mn_{14}O_{27} \cdot 7.9H_2O$. Meanwhile, the semicircles of $Mg_{0.9}Mn_3O_7 \cdot 2.7H_2O$, corresponding to R_{ct} of 38.27 Ω and 31.07 Ω at initial and cycled states, respectively, are also lower than those (initial state: 55.04 Ω and cycled state: 67.23 Ω) of δ-$Mg_2Mn_{14}O_{27} \cdot 7.9H_2O$. Therefore, considering systematically evaluated electrochemical kinetics of both electrodes under identical conditions, it is convincible that the new geometric stacking orders of edge-sharing MnO_6 layers and intrinsic MgO_6 layers in $Mg_{0.9}Mn_3O_7 \cdot 2.7H_2O$ is more favorable for charge storage compared to conventional ribbon-like ordered MnO_6 co-planes along with perishable "pillars" of δ-MnO_2 in AZIBs system.

2.4. H+/Zn2+ Electrochemical Reaction Mechanism

To gain further mechanistic insight of structural evolution for $Mg_{0.9}Mn_3O_7 \cdot 2.7H_2O$ and δ-$Mg_2Mn_{14}O_{27} \cdot 7.9H_2O$, multiple in situ and ex situ characterizations of the electrodes upon varied (dis)charge states. The ex situ SEM images and EDS of both Mg involved layered manganese oxide cathodes were detected to determine elemental ratio variations and morphology changes at multiple stages, which display different results regarding to Mg species content within the electrodes. As for $Mg_{0.9}Mn_3O_7 \cdot 2.7H_2O$, it is seen that there are no prominent changes of Mg:Mn ratio ($\approx 0.7:3$) upon varied charge/discharge states (**Figure** 4a,b, and S7a, Supporting Information). In contrast, no trace signals of Mg were found in all states of

δ-$Mg_2Mn_{14}O_{27} \cdot 7.9H_2O$ electrode after the cycling test, implying an absence of deliberately introduced "pillar" ion in the framework (Figure S8a, Supporting Information). Meanwhile, a dramatically increased zinc species during the discharge process along with flakes crystal occurring on the surface of both electrodes indicate the generation of $Zn_4SO_4(OH)_6 \cdot 5H_2O$ (ZHS) especially when the working voltage is close to fully discharged state. Furthermore, this precipitation is reversible and can disappear as the working voltage rise during the charging process, which can be also identified by XRD characterizations in the following content. The phenomena have been extensively characterized in Mn-based cathode for AZIBs owing to the localized pH increase on the neighboring surface of electrodes via the depletion of the proton.[48] Additionally, ex situ XPS results of $Mg_{0.9}Mn_3O_7 \cdot 2.7H_2O$ electrodes were presented in Figures 4c and S7b,c, Supporting Information, to further validate the change of elemental composition and valence states upon fully charge/discharge processes. The core-level Mn $2p_{3/2}$ spectra clearly reveal a reversible oxidization and reduction of Mn species at charge and discharge states, respectively, manifesting as the reversible shift of the binding energy from 641.9 eV to 641.6 eV agreed with previously reported redox pairs of $Mn^{3+/4+}$ species.[49] Moreover, the core-level spectra of Zn 2p and Mg 1s clearly indicate the inserted zinc species vary with signal intensities, and steady Mg^{2+} content exists in the (dis)charge electrodes (Figures 4c and S7b,c, Supporting Information). While it is also observed that there is a reversible redox pair of $Mn^{3+/4+}$ species along with varied strength of Zn 2p signals upon (dis)charge processes in the electrodes of δ-$Mg_2Mn_{14}O_{27} \cdot 7.9H_2O$ characterized from Mn/Zn 2p core-level and survey spectra, respectively. However, there is still no Mg species appearing in these electrodes. These results further confirm the unstable feature of pillar ions in δ-phase MnO_2 (Figures S8b and S9a,b, Supporting Information) and which agreed well with the previous observation of Na^+ leaching from the layered MnO_2 host during electrochemical reactions.[20,50]

In addition to elemental characterizations, Figure 4d demonstrates the structural evaluation of $Mg_{0.9}Mn_3O_7 \cdot 2.7H_2O$ at varied (dis)charge states via ex situ XRD. It is seen that all characteristic peaks corresponding to $Mg_{0.9}Mn_3O_7 \cdot 2.7H_2O$ can be easily identified from the plots. Meanwhile, newly emerged diffraction peaks are well-indexed with ZHS (JCPDS No. 44–0674) at both discharge states of 0.9 V in 1st and 20th cycled electrodes, in line with the results from SEM images. Moreover, there are neglectable shifts (from 5.91° to 5.83°) of the (003) diffraction peak after the battery discharge, and then reversibly return to 5.91° at the 20th charged state, implying a superior reversibility of crystallographic structures and ≈1% lattice volume changes upon the H^+ and Zn^{2+} (de)intercalation. Whereas the δ-$Mg_2Mn_{14}O_{27} \cdot 7.9H_2O$ electrode experienced more significant changes of d-spacing of (001) plane along c-axis reflecting a relatively irreversible shift of peaks from 4.7° to 3.9° (Δd-spacing = 1.8 Å) at the 1st and 20th charged states, respectively, accompanying with gradually broader full width at half maximum compared with the peak located at 4.2° as for the pristine electrode (Figure S9c, Supporting Information), which indicates a relatively large volume changes along with increased chaos of crystal lattices upon cycling treatments. Furthermore, ZHS can be identified at fully discharged states
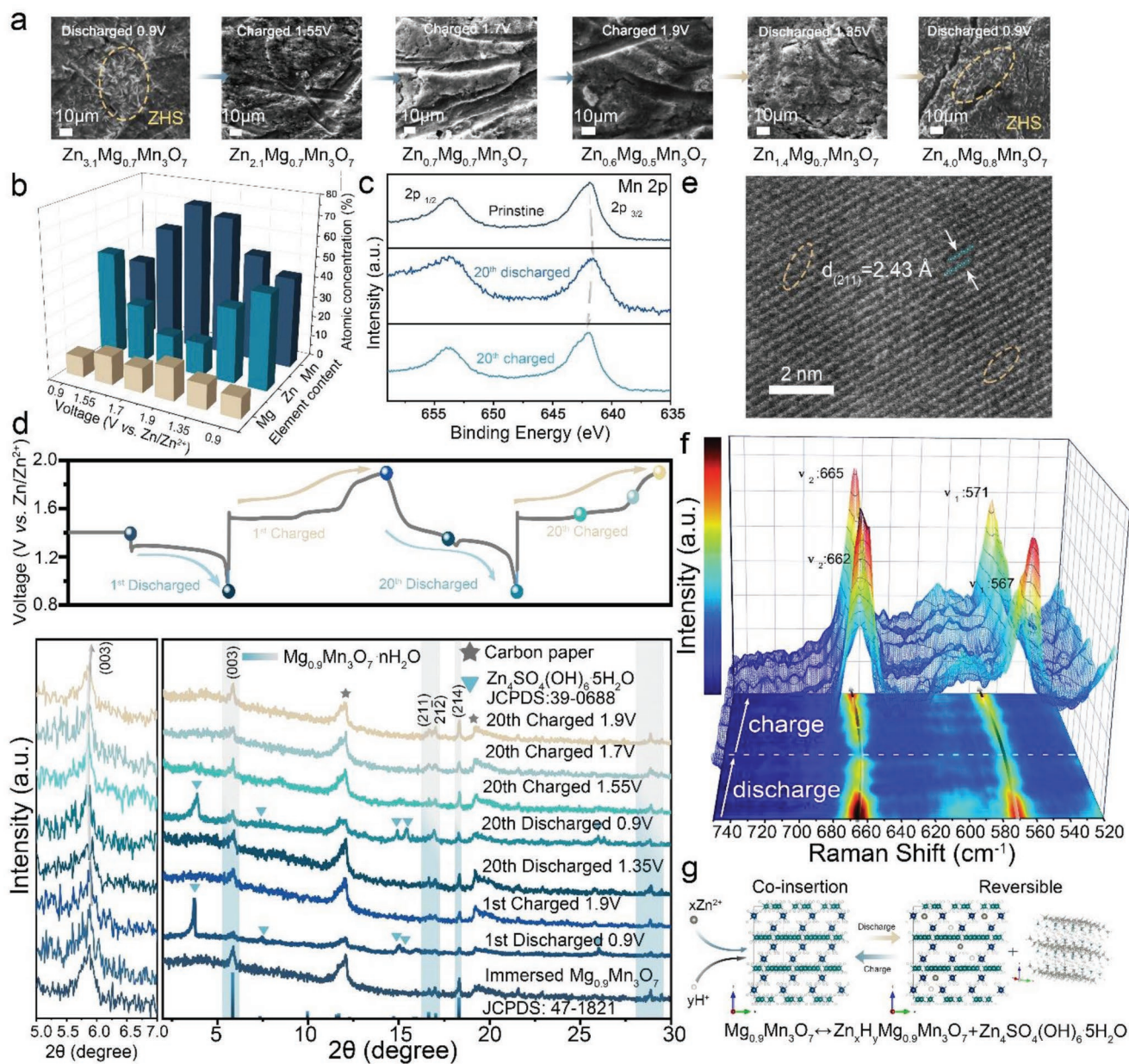
Figure 4. Ex situ characterizations on $Mg_{0.9}Mn_3O_7\cdot2.7H_2O$ electrodes: a) SEM images of the electrodes. b) Calculated elemental ratios upon various (dis)charge states through SEM-EDS results. c) XPS spectra of Mn 2p at (dis)charged states. d) XRD patterns at different (dis)charged states. e) HAADF-STEM image of the discharge state. f) In situ Raman spectra of $Mg_{0.9}Mn_3O_7\cdot2.7H_2O$. g) Schematic illustration of the charge storage mechanism of $Mg_{0.9}Mn_3O_7\cdot2.7H_2O$ in AZIBs. (Dark green, dark blue, silver and small grey spheres refer to Mn, Mg, Zn, and O atoms).

in δ-$Mg_2Mn_{14}O_{27}\cdot7.9H_2O$ electrodes, and it can vanish upon charge processes. Figure 4e exhibits the HAADF-STEM image referring to the fully discharged state of $Mg_{0.9}Mn_3O_7\cdot2.7H_2O$, in which the intercalated zinc ions with slightly expanded d-spacing (2.43 Å) of the lattice fringe corresponding to the (211) plane shows the consistent change as observed from XRD characterizations. Also, in situ Raman spectra were carried out to further determine the structural evolution (Figure 4f). Comparably, the vibration modes of manganese oxides have two characteristic bands sensitive to the layered framework. The one (v_1) at ≈570 to 590 cm^{-1} attributes to Mn–O stretching

mode of the basal plane within octahedral MnO_6 layers, whereas the other one (v_2) shows up ≈620–680 cm^{-1} referring to Mn–O symmetric stretching vibration in octahedral MnO_6.[51] It is also verified that the distinguishable features with strong intensities exist in $Mg_{0.9}Mn_3O_7\cdot2.7H_2O$ at the positions of 571 and 665 cm^{-1}, respectively, at fully charged states. During the discharge process, both peaks belonging to the two vibration modes gradually become weaker, especially at the fully discharged state, which is in agreement with previously reported alkali ion inserted δ-MnO_2, attributing to structural change induced varied phonon properties upon Zn^{2+}/H^+

**ADVANCED
SCIENCE NEWS**

www.advancedsciencenews.com

**ADVANCED
ENERGY
MATERIALS**

www.advenergymat.de

intercalation.[52] Meanwhile, it is also observed that both vibration modes have slight redshifts to 567 and 662 cm^{-1} during discharge processes suggesting a reduction of Mn(IV) species in octahedral MnO$_6$. Reversibly, the Raman peaks experience blueshift upon following charge processes and finally reach to the same position, demonstrating its superior structural stability. In contrast to the reversible changes of Raman vibration modes in Mg$_{0.9}$Mn$_3$O$_7$·2.7H$_2$O, the bands at 668 cm^{-1} and 498 cm^{-1} standing for the out-plane Mn-O stretching vibration modes in pristine δ-Mg$_2$Mn$_{14}$O$_{27}$·7.9H$_2$O present dramatical redshifts at the 10th fully charged state (660 cm^{-1}), and more offset (658 cm^{-1}) were characterized at 20th fully charged state, suggesting gradually softening photon modes presumably derived from irreversible local coordination environment in the lattice and chemical states (Figure S10a, Supporting Information). Similarly, it is seen that there are more significant red shifts occurring in discharged states of the 10th and 20th cycles for δ-Mg$_2$Mn$_{14}$O$_{27}$·7.9H$_2$O electrodes, respectively, along with newly emerging broad peaks at 289–345 cm^{-1} (Zn–O stretching modes). The results indicate an insertion of Zn^{2+}/H$^+$, which agree with previous Raman spectroscopic studies on intercalated δ-MnO$_2$.[52,53]

Additionally, the inductively coupled plasma optical emission spectrometry (ICP-OES) analysis of the Mn species concentration in a cycled 3 M ZnSO$_4$ electrolyte exhibits that the dissolution of Mn species could be significantly alleviated in Mg$_{0.9}$Mn$_3$O$_7$·2.7H$_2$O cathode after 10 and 20 cycles, respectively, at fully discharged states (Figure S10b, Supporting Information). While the δ-Mg$_2$Mn$_{14}$O$_{27}$·7.9H$_2$O cathode presents a higher concentration of Mn species in the electrolyte after the cycling test, implying more serious structural Mn dissolution issues.

Overall, through the discussion on the structural and chemical evolutions of Mg$_{0.9}$Mn$_3$O$_7$·2.7H$_2$O and δ-Mg$_2$Mn$_{14}$O$_{27}$·7.9H$_2$O, the reaction mechanism of Mg$_{0.9}$Mn$_3$O$_7$·2.7H$_2$O is similar to that of δ-Mg$_2$Mn$_{14}$O$_{27}$·7.9H$_2$O as a co-insertion/extrusion of Zn^{2+}/H$^+$ demonstrated in Figure 4g. It is obviously seen that the new geometric orders of octahedral MnO$_6$ layers and intrinsically stable Mg coordination in Mg$_{0.9}$Mn$_3$O$_7$·2.7H$_2$O can effectively protect the host framework from the structural failure after coinsertion, such as disordered lattice and Mn dissolution/migration as observed in δ-Mg$_2$Mn$_{14}$O$_{27}$·7.9H$_2$O, which can result in a fast capacity fade.

2.5. DFT Simulations

To gain deep insights into geometric and electronic structure variations of Mg$_{0.9}$Mn$_3$O$_7$·2.7H$_2$O during the electrochemical process, DFT calculations were conducted. The structure of bulk MgMn$_3$O$_7$·3H$_2$O are calculated, which is exhibited in **Figure 5**a. It is further confirmed that the structure consists of two-dimensional MnO$_6$ octahedral layers where 1/7 of the Mn atoms are removed orderly in the (001) direction (Mn$_3$O$_7$ layers) and a layer of Mg^{2+} is located between Mn$_3$O$_7$ layers to form Mg-□Mn-Mg dumbbell superstructural motif. Moreover, Mn, O1, O2, and WO (WO refers to the oxygen from the bounding water) locate on Wyckoff positions 18f, and Mg and O3 are on Wyckoff positions 6c. One Mg^{2+} cation is bonded to three

equivalent O2 and three equivalent MO atoms that come from the molecular water to form MgO$_6$ octahedra that share corners with six equivalent MnO$_6$ octahedra. The electronic structure of MgMn$_3$O$_7$·3H$_2$O including the partial density of states (PDOS) and band structures are also calculated and projected in Figure 5b,c. For the valence band top, the 2p orbitals of O made the major contribution, while the 3d orbitals of Mn primarily locate above the Fermi level. The electrons of 3p (Mg) and 2p(O) hybridize with the 3d orbitals of Mn^{4+} at the valence band top and conduction band bottom. The band gap is indirect from A to H in Figure 5c and indicates its semiconductive nature. The band gap value of MgMn$_3$O$_7$·3H$_2$O is 2.13 eV. The Mg defective MgMn$_3$O$_7$·3H$_2$O (Mg$_{0.9}$Mn$_3$O$_7$·2.7H$_2$O) was also considered based on our experimental results that the as-prepared material is inherently flawed. Mg$_{0.9}$Mn$_3$O$_7$·2.7H$_2$O are built from Mg$_6$Mn$_{18}$O$_{42}$·15H$_2$O where one Mg is removed. Hence, the calculated host for subsequent intercalations of Zn complies with Mg$_5$Mn$_{18}$O$_{42}$·15H$_2$O. All possible insertion sites are considered and screened by the calculated total energies of the structures. As shown in Figure 5a, the first inserted Zn prefers to accommodate at the previous Mg point vacancy site. The second one is still close to the Mg vacancy and forms an irregular ZnO$_4$ tetrahedron with one O from the previous MgO$_6$ octahedra. In ZnO$_4$, there is one corner connected with the O of MgO$_5$, which also makes one H transfer to the other MnO$_6$ and increases the Mn–O bond length. During the third Zn insertion, it locates on the top site of the first Zn and slightly attracts the first Zn in (001) orientation. In the end, the fourth Zn enters into the middle of MgO$_5$ and the third Zn. All four Zn uniformly inserted into the sites are surrounded by Mg vacancy. During the whole intercalation process, the interlayer spacings of Zn$_x$Mg$_5$Mn$_{18}$O$_{42}$·15H$_2$O (x = 1–4) have remained virtually unchanged (Figure 5d) and the average interlayer spacing is 6.97 Å, further verifying its robust character as quasi-zero strain hosts for zinc storage. This is mainly due to the hydrogen bonds and MgO$_6$ acting as pillars between Mn$_3$O$_7$ layers, which is beneficial for reversible charge/discharge processes.

In addition, Nam et al. also verified that an interlayer spacing of ≈7 Å could alleviate Mn dissolution in crystal water accommodated δ-MnO$_2$ since a higher diffusion barrier has to overcome.[54] In contrast, for a larger interlayer spacing (>10 Å), Mn^{2+} could migrate into the electrolyte during Zn^{2+} insertion as the trend is energetically and kinetically favorable, which takes responsibility for capacity fading in manganese oxides. As the results, ab initio molecular dynamics (AIMD) simulations were adopted for the 111-atom supercell of Zn$_1$Mg$_5$Mn$_{18}$O$_{42}$·15H$_2$O at 300 K in the NVT ensemble, which indicate that Zn insertion is unable to cause Mn diffusion in the host and significant structural distortion (Figures S11 and S12, Supporting Information), which is varied from conventional layered MnO$_2$ with respect to significant MnO$_6$ distortion for forming Zn–Mn "dumbbell" superstructures (Figure S13, Supporting Information).

The average Mn-O bond changes are also illustrated in Figure 5d, those bond length changes less than 0.1 Å are generally ignored, For Mg$_6$Mn$_{18}$O$_{42}$·15H$_2$O, Mg$_5$Mn$_{18}$O$_{42}$·15H$_2$O, and Zn$_1$Mg$_5$Mn$_{18}$O$_{42}$·15H$_2$O, the Mn-O bond change is zero. After two Zn^{2+} are inserted, there is a reduction of Mn^{4+} along with the occurrence of the Jahn–Teller effect. The Mn-O bond variations compared to Mg$_6$Mn$_{18}$O$_{42}$·15H$_2$O

**ADVANCED
SCIENCE NEWS**

www.advancedsciencenews.com

**ADVANCED
ENERGY
MATERIALS**

www.advenergymat.de
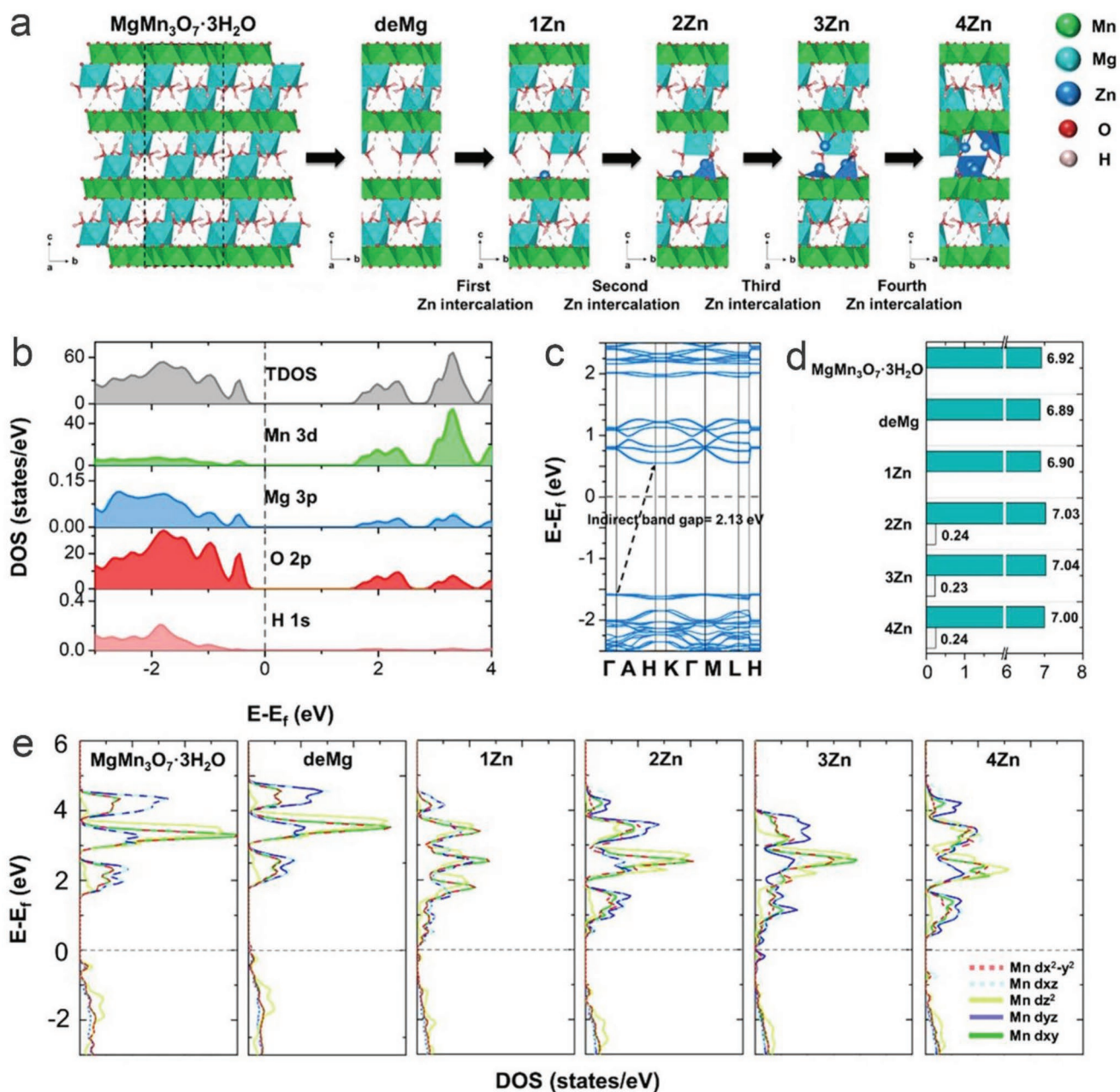
Figure 5. a) The optimized structures of bulk $MgMn_3O_7 \cdot 3H_2O$, $Mg_{0.9}Mn_3O_7 \cdot 2.7H_2O$, and $Mg_{0.9}Mn_3O_7 \cdot 2.7H_2O$ with Zn intercalation. b) The partial density of states (PDOS) of $MgMn_3O_7 \cdot 3H_2O$. c) The band structures of $MgMn_3O_7 \cdot 3H_2O$. d) The histogram of interlayer spacings and Mn–O bond length changes in $MgMn_3O_7 \cdot 3H_2O$, $Mg_{0.9}Mn_3O_7 \cdot 2.7H_2O$, and $Mg_{0.9}Mn_3O_7 \cdot 2.7H_2O$ with Zn intercalation. The turquoise columns are interlayer spacings, while the white columns are Mn–O bond length changes. e) The partial density of states (PDOS) of Mn in $MgMn_3O_7 \cdot 3H_2O$, $Mg_{0.9}Mn_3O_7 \cdot 2.7H_2O$, and $Mg_{0.9}Mn_3O_7 \cdot 2.7H_2O$ with Zn intercalation. Those dotted lines in PDOS and band structures are Fermi levels.

in $Zn_2Mg_5Mn_{18}O_{42} \cdot 15H_2O$, $Zn_3Mg_5Mn_{18}O_{42} \cdot 15H_2O$, and $Zn_4Mg_5Mn_{18}O_{42} \cdot 15H_2O$ are 0.24, 0.23 and 0.24 Å, respectively. The above results indicate this continuous reduction as Zn insertion cannot cause severe the Jahn–Teller effect, that is, less Mn species loss during the discharge process.

The PDOS of $Mg_6Mn_{18}O_{42} \cdot 15H_2O$, $Mg_5Mn_{18}O_{42} \cdot 15H_2O$, and $Zn_xMg_5Mn_{18}O_{42} \cdot 15H_2O$ ($x = 1$–4) have also been illustrated in Figure 5e. The insertion of Zn indicates a considerable enhancement in the electrical conductivity with the shrinkage

of the band gap. There are all Mn^{4+}, the dx^2-y^2, dz^2, and dxy are occupied in $Mg_6Mn_{18}O_{42} \cdot 15H_2O$. With the reduction caused by Zn insertion, the electrons will gradually occupy the dyz and dxz, and the mixture of dyz and dxz peak appears obviously in the PDOS of 2 Zn for the first Zn balance the value state change of the Mg defect. Then, the continuous intercalation of Zn gradually increases the dyz and dxz mixed peak around the Fermi level and greatly improved electronic conductivity by narrowing the band gap.

3. Conclusion

In summary, this study demonstrates that new superstructural 2D manganese (IV) oxides, $Mg_{0.9}Mn_3O_7 \cdot 2.7H_2O$, possess pinned MgO_6 layers and built-in Mn vacancy within its distinguishable layers along with interlaminar hydrogen bond reinforcement. This cathode material can deliver a high specific capacity of 312 mAh g^{-1} at 0.2 A g^{-1} and outstanding cycling stability of 92% capacity retention after 5000 cycles at 5 A g^{-1}. Meanwhile, superior rate capabilities and quasi-zero volumetric change of the lattice structures further verify its feasibility as a promising cathode host in practical applications. Importantly, through a detailed comparison with typical δ-MnO_2 with various pre-intercalated cations, we proposed a solution to meet the unstable nature of pillar cations caused by loose electrostatic interactions and serious manganese dissolution from the structural disorder. Thus, a new paradigm of 2D material is successfully developed in this study, which could offer more inspiration on modulation of geometric orders on both octahedral MnO_6 and pillar ions layers in superstructural materials for high-performance AZIBs application.

Supporting Information

Supporting Information is available from the Wiley Online Library or from the author.

Acknowledgements

Conflict of Interest

The authors declare no conflict of interest.

Author contribution

J.L. and N.L. contributed equally to this work. J.L. and G.H. conceived the project and devised experiments; J.L. prepared the materials and conducted all experimental studies with the support from F.Z., Y.J., and T.M.; L.K. performed characterization of morphology; N.L. and G.C. performed theoretical calculations; G.H. directed this project; M.W., I.P., P.S., D.B., G.C., and G.H. supervised the project; J.L., N.L. and G.H. wrote the manuscript.

Data Availability Statement

The data that support the findings of this study are available from the corresponding author upon reasonable request.

Keywords

[1] C. Li, X. Xie, S. Liang, J. Zhou, *Energy Environ. Mater.* **2020**, *3*, 146.
[2] Z. Chen, F. Mo, T. Wang, Q. Yang, Z. Huang, D. Wang, G. Liang, A. Chen, Q. Li, Y. Guo, X. Li, J. Fan, C. Zhi, *Energy Environ. Sci.* **2021**, *14*, 2441.
[3] L. Chen, Q. An, L. Mai, *Adv. Mater. Interfaces* **2019**, *6*, 1900387.
[4] B. Tang, L. Shan, S. Liang, J. Zhou, *Energy Environ. Sci.* **2019**, *12*, 3288.
[5] S. Liu, L. Kang, J. M. Kim, Y. T. Chun, J. Zhang, S. C. Jun, *Adv. Energy Mater.* **2020**, *10*, 2000477.
[6] T. Wang, C. Li, X. Xie, B. Lu, Z. He, S. Liang, J. Zhou, *ACS Nano* **2020**, *14*, 16321.
[7] J. Ming, J. Guo, C. Xia, W. Wang, H. N. Alshareef, *Mater. Sci. Eng., R Rep.* **2019**, *135*, 58.
[8] V. Mathew, B. Sambandam, S. Kim, S. Kim, S. Park, S. Lee, M. H. Alfaruqi, V. Soundharrajan, S. Islam, D. Y. Putro, J. Hwang, Y. Sun, J. Kim, *ACS Energy Lett.* **2020**, *5*, 2376.
[9] Y. Zhao, Y. Zhu, X. Zhang, *InfoMat.* **2020**, *2*, 237.
[10] D. Chen, M. Lu, D. Cai, H. Yang, W. Han, *J. Energy Chem.* **2021**, *54*, 712.
[11] X. Wang, Z. Zhang, B. Xi, W. Chen, Y. Jia, J. Feng, S. Xiong, *ACS Nano* **2021**, *15*, 9244.
[12] X. Jia, C. Liu, Z. G. Neale, J. Yang, G. Cao, *Chem. Rev.* **2020**, *120*, 7795.
[13] Y. Li, D. Zhang, S. Huang, H. Ying, *Nano Energy* **2021**, *85*, 105969.
[14] J. E. Post, *Proc. Natl. Acad. Sci. USA* **1999**, *96*, 3447.
[15] L. E. Blanc, D. Kundu, L. F. Nazar, *Joule* **2020**, *4*, 771.
[16] T. Xiong, Y. Zhang, W. Siang, V. Lee, J. Xue, *Adv. Energy Mater.* **2020**, *10*, 2001769.
[17] H. S. Choi, S. J. Kim, J. J. Kim, *Geosci. J.* **2004**, *8*, 273.
[18] Y. Liu, Y. Qiao, W. Zhang, H. Wang, K. Chen, H. Zhu, Z. Li, Y. Huang, *J. Mater. Chem. A* **2015**, *3*, 7780.
[19] H. T. Zhu, J. Luo, H. X. Yang, J. K. Liang, G. H. Rao, J. B. Li, Z. M. Du, *J. Phys. Chem. C* **2008**, *112*, 17089.
[20] L. Athouël, F. Moser, R. Dugas, O. Crosnier, D. Bélanger, T. Brousse, *J. Phys. Chem. C* **2008**, *112*, 7270.
[21] P. Simon, Y. Gogotsi, *Nat. Mater.* **2021**, *20*, 1597.
[22] E. Mccalla, S. Jia, *Nat. Sustain.* **2022**, *5*, 181.
[23] Y. Li, S. Zhu, Z. Liu, *J. Am. Chem. Soc.* **2016**, *138*, 5371.
[24] R. A. House, U. Maitra, M. A. Pérez-osorio, J. G. Lozano, L. Jin, J. W. Somerville, L. C. Duda, A. Nag, A. Walters, K. Zhou, M. R. Roberts, P. G. Bruce, *Nature* **2020**, *577*, 502.
[25] Y. Haraguchi, A. Matsuo, K. Kindo, Z. Hiroi, *Phys. Rev. B* **2018**, *98*, 064412.
[26] Q. Zhang, X. He, J. Shi, N. Lu, H. Li, Q. Yu, Z. Zhang, L. Chen, B. Morris, Q. Xu, P. Yu, *Nat. Commun.* **2017**, *8*, 104.
[27] B. Mortemard de Boisse, S.i. Nishimura, E. Watanabe, L. Lander, A. Tsuchimoto, J. Kikkawa, E. Kobayashi, D. Asakura, M. Okubo, A. Yamada, *Adv. Energy Mater.* **2018**, *8*, 1800409.
[28] Y. Song, Q. Pan, H. Lv, D. Yang, Z. Qin, M. Zhang, X. Sun, X. Liu, *Angew. Chem., Int. Ed.* **2021**, *60*, 5718.
[29] N. Zhang, F. Cheng, J. Liu, L. Wang, X. Long, X. Liu, F. Li, J. Chen, *Nat. Commun.* **2017**, *8*, 405.
[30] J. Li, K. McColl, X. Lu, S. Sathasivam, H. Dong, L. Kang, Z. Li, S. Zhao, A. G. Kafizas, R. Wang, D. J. L. Brett, P. R. Shearing, F. Corà, G. He, C. J. Carmalt, I. P. Parkin, *Adv. Energy Mater.* **2020**, *10*, 2000058.

ADVANCED
SCIENCE NEWS

www.advancedsciencenews.com

ADVANCED
ENERGY
MATERIALS

www.advenergymat.de

[31] N. Zhang, X. Chen, M. Yu, Z. Niu, F. Cheng, J. Chen, *Chem. Soc. Rev.* **2020**, *49*, 4203.

[32] W. Sun, F. Wang, S. Hou, C. Yang, X. Fan, Z. Ma, T. Gao, *J. Am. Chem. Soc.* **2017**, *139*, 9775.

[33] Q. Xie, G. Cheng, T. Xue, L. Huang, S. Chen, *Mater. Today Energy* **2022**, *24*, 100934.

[34] W. Shi, S. Vincent, J. Xue, *ChemSusChem* **2021**, *14*, 1634.

[35] G. Fang, C. Zhu, M. Chen, J. Zhou, B. Tang, X. Cao, X. Zheng, A. Pan, S. Liang, *Adv. Funct. Mater.* **2019**, *29*, 1808375.

[36] N. Zhang, F. Cheng, Y. Liu, Q. Zhao, K. Lei, C. Chen, X. Liu, J. Chen, *J. Am. Chem. Soc.* **2016**, *138*, 12894.

[37] V. Soundharrajan, B. Sambandam, S. Kim, V. Mathew, J. Jo, S. Kim, J. Lee, S. Islam, K. Kim, Y. Sun, J. Kim, *ACS Energy Lett.* **2018**, *3*, 1998.

[38] B. Jiang, C. Xu, C. Wu, L. Dong, J. Li, F. Kang, *Electrochim. Acta* **2017**, *229*, 422.

[39] C. Zhu, G. Fang, J. Zhou, J. Guo, Z. Wang, C. Wang, J. Li, Y. Tang, S. Liang, *J. Mater. Chem. A* **2018**, *6*, 9677.

[40] B. Wu, G. Zhang, M. Yan, T. Xiong, P. He, L. He, X. Xu, L. Mai, *Small* **2018**, *14*, 1703850.

[41] D. Kundu, B. D. Adams, V. Duffort, S. H. Vajargah, L. F. Nazar, *Nat. Energy* **2016**, *1*, 16119.

[42] C. Xia, J. Guo, P. Li, X. Zhang, H. N. Alshareef, *Angew. Chem., Int. Ed.* **2018**, *57*, 3943.

[43] P. Hu, T. Zhu, X. Wang, X. Wei, M. Yan, J. Li, W. Luo, W. Yang, W. Zhang, L. Zhou, Z. Zhou, L. Mai, *Nano Lett.* **2018**, *18*, 1758.

[44] L. Zhang, L. Chen, X. Zhou, Z. Liu, *Adv. Energy Mater.* **2015**, *5*, 1400930.

[45] V. Renman, D. O. Ojwang, M. Valvo, C. P. Gomez, T. Gustafsson, G. Svensson, *J. Power Sources* **2017**, *369*, 146.

[46] G. Kasiri, J. Glenneberg, A. Bani, R. Kun, F. La, *Energy Storage Mater.* **2019**, *19*, 360.

[47] F. Ming, H. Liang, Y. Lei, S. Kandambeth, M. Eddaoudi, H. N. Alshareef, *ACS Energy Lett.* **2018**, *3*, 2602.

[48] P. Oberholzer, E. Tervoort, A. Bouzid, A. Pasquarello, D. Kundu, *ACS Appl. Mater. Interfaces* **2019**, *11*, 674.

[49] E. S. Ilton, J. E. Post, P. J. Heaney, F. T. Ling, S. N. Kerisit, *Appl. Surf. Sci.* **2016**, *366*, 475.

[50] H. Dong, J. Li, S. Zhao, Y. Jiao, J. Chen, Y. Tan, D. J. L. Brett, G. He, I. P. Parkin, *ACS Appl. Mater. Interfaces* **2021**, *13*, 745.

[51] Z. Morgan, D. A. Kitchaev, J. Nelson, C. Schnedermann, K. Lim, G. Ceder, W. Tumas, M. F. Toney, D. G. Nocera, *Proc. Natl. Acad. Sci. USA* **2018**, *115*, E5261.

[52] D. Chen, D. Ding, X. Li, G. H. Waller, X. Xiong, M. A. El-Sayed, M. Liu, *Chem. Mater.* **2015**, *27*, 6608.

[53] G. Wang, Y. Wang, B. Guan, J. Liu, Y. Zhang, X. Shi, C. Tang, G. Li, Y. Li, X. Wang, L. Li, *Small* **2021**, *17*, 2104557.

[54] K. W. Nam, H. Kim, J. K. Choi, J. W. Choi, *Energy Environ. Sci.* **2019**, *12*, 1999.

2201840 (12 of 12)